Chemical Tomography in a Fresh Wildland Fire Plume: a Large Eddy Simulation (LES) Study

Siyuan Wang,[1,2,3,*] Matthew M. Coggon,[1,2] Georgios I. Gkatzelis,[1,2,†] Carsten Warneke,[1,2] Ilann Bourgeois,[1,2] Thomas Ryerson,[2] Jeff Peischl,[1,2] Patrick R. Veres,[2] J. Andrew Neuman,[1,2] Johnathan Hair,[4] Taylor Shingler,[4] Marta Fenn,[4] Glenn Diskin,[4] L. Greg Huey,[5] Young Ro Lee,[5] Eric C. Apel,[3] Rebecca S. Hornbrook,[3] Alan J. Hills,[3] Samuel R. Hall,[3] Kirk Ullmann,[3] Megan M. Bela,[1,2] Michael K. Trainer,[1,2] Rajesh Kumar,[6] John J. Orlando,[3] Frank M. Flocke,[3] Louisa K. Emmons,[3]

[1] Cooperative Institute for Research in Environmental Sciences (CIRES), University of Colorado, Boulder, Colorado
[2] National Oceanic and Atmospheric Administration (NOAA), Chemical Sciences Laboratory (CSL), Boulder, Colorado
[3] National Center for Atmospheric Research (NCAR), Atmospheric Chemistry Observations and Modeling Laboratory (ACOM), Boulder, Colorado
[4] National Aeronautics and Space Administration, Langley Research Center, Hampton, Virginia
[5] School of Earth and Atmospheric Sciences, Georgia Institute of Technology, Atlanta, Georgia
[6] National Center for Atmospheric Research (NCAR), Research Applications Laboratory (RAL), Boulder, Colorado

* Corresponding author: Siyuan Wang (siyuan.wang@noaa.gov)
Cooperative Institute for Research in Environmental Sciences (CIRES), University of Colorado, Boulder, Boulder, Colorado
NOAA, Chemical Sciences Laboratory (CSL)
325 Broadway, Boulder, CO

† Now at: Institute of Energy and Climate Research, IEK-8: Troposphere, Forschungszentrum Jülich GmbH, Jülich, Germany

30

31 **KEY POINTS**

32 1. Photochemistry is active at the edges of thick fire plumes, while dark chemistry is present
33 in the lower part and below thick plumes
34 2. Hydroxyl radicals formed from nitrous acid drive the plume oxidation. Nitrous acid may
35 be produced on aerosols
36 3. Model spatial resolution affects chemical regime; sufficiently high spatial resolution (e.g.,
37 1 km) is needed to capture the impacts of wildfires on air quality

38

ABSTRACT

Wildland fires involve complicated processes that are challenging to represent in chemical transport models. Recent airborne measurements reveal remarkable chemical tomography in fresh wildland fire plumes, which remain yet to be fully explored using models. Here we present a high-resolution large eddy simulation (LES) model coupled to chemistry to study the chemical evolution in fresh wildland fire plume. The model is configured for a large fire heavily sampled during the Fire Influence on Regional to Global Environments and Air Quality (FIREX-AQ) field campaign, and a variety of airborne measurements are used to evaluate the chemical heterogeneity revealed by the model. We show that the model captures the observed cross-transect variations of a number of compounds quite well, including ozone (O_3), nitrous acid (HONO), and peroxyacetyl nitrate (PAN), etc. The combined observational and modeling results suggest that the top and edges of fresh plume drive the photochemistry, while dark chemistry is also present but in the lower part of the plume. The model spatial resolution is shown to be very important as it may shift the chemical regime, leading to biases in O_3 and NO_x chemistry. Based on findings in this work, we speculate that the impact of small fires on air quality may be largely underestimated in models with coarse spatial resolutions.

PLAIN LANGUAGE SUMMARY

Recent fire seasons in the United States have been record-setting for many states. Several large wildfires raged across the entire west coast, and lofted smoke plumes spread to the majority of the continental U.S. From a scientific perspective, wildland fires are fascinating due to their complexity. Fires emit heat, creating a plume of hot and turbulent air. The fire plume also contains many gases and aerosol particles produced from the burning and baking of a variety of fuels on the ground (trees, grasses, leaf letter and other fallen debris, etc). Many of these gases and aerosol particles can impact climate, air quality, and human health. For this reason, most modern air quality and climate models now consider wildland fires. However, wildland fires are fundamentally challenging for these models, because many fine-scale and large-scale processes are entangled at the same time. In this work, we use a high resolution turbulence-resolving numerical model to study the fine details in a wildland fire plume, with implications for large-scale air quality and climate models.

KEYWORDS

Biomass burning, wildland fire, large eddy simulation, airborne measurements, ozone, nitrous acid, peroxyacetyl nitrate

1. INTRODUCTION

Wildland fires are a natural phenomenon and an important component of the global ecosystem. Although the global trends of wildland fires remain a subject of debate (Doerr & Santín, 2016), the projected burned area and the fire season length are expected to increase in the 21st century, especially in the Northern Hemisphere (Doerr & Santín, 2016; Flannigan et al., 2013). In the United States, wildland fires are a growing concern. Records have shown that large wildfire activity in the United States increased suddenly in the mid-1980s, with higher large-fire frequency, longer wildfire durations, and longer wildfire seasons (Westerling et al., 2006), largely driven by human-caused climate change (Abatzoglou & Williams, 2016).

Wildland fires often pose considerable risks to human health and property, with major impacts on air quality and the climate system. A 2010 survey showed that 32% of the U.S. population reside in "wildland-urban interface areas", which are defined as areas where structures and other human development meet or intermingle with undeveloped wildland and where wildfires have their greatest impacts on people (Martinuzzi et al., 2015). Wildland fires emit a wide range of pollutants and greenhouse gases, such as particulate matters, carbon monoxide (CO), carbon dioxide (CO_2), volatile organic compounds (VOCs), and reactive nitrogen species (Liu et al., 2017), many of which produce secondary pollutants such as ozone (O_3) and secondary organic aerosols in the atmosphere (Hodshire et al., 2019; Jaffe et al., 2020; Lu et al., 2016; Palm et al., 2020). Growing evidence indicates that wildfire smoke exposure is associated with respiratory morbidity and potentially cardiovascular morbidity as well (Colleen et al., 2016). Efforts to improve air quality in the U.S. show some promising trends as evidenced from improvements in fine particulate matter pollution in the majority of the U.S. over the past

96 decades, except in the wildfire-prone regions where air quality has been worsening due to
97 wildfire events (Jaffe et al., 2020; McClure & Jaffe, 2018). Given the broad impacts they have on
98 the atmosphere and the climate system, wildland fires are a vital component in most modern
99 chemical transport models and climate models.

100 The scope of wildland fires ranges from microscale to mesoscale, with influence from both
101 microphysics and chemistry. Wildland fires also involve complicated feedback mechanisms, e.g.,
102 the fire source and plume alter the flow field and the radiation in the atmosphere; in turn, the
103 meteorology, terrain, and the fuels also affect the fire behavior. As a result, wildland fires are
104 challenging to model. State-of-the-art fire models have been developed to explicitly solve the
105 two-way coupling between weather and fire behavior (Coen, 2013; Mandel et al., 2011).
106 However, models with realistic representations of the two-way coupling with the land/fuel
107 models and the fire-weather interactions are often highly complex and rather computationally
108 demanding, even more so if coupled with chemistry. Most air quality and climate models are not
109 designed to accommodate such complexity. Because of the computational concerns, many air
110 quality/climate models are operated at coarse spatial resolutions and with longer integration
111 time steps. As a result, many key physical and chemical processes (e.g., heat release and plume
112 rise) cannot be explicitly modeled, and hence rely on subgrid parameterizations. This presents a
113 gap between “what is happening” and “what is coded in air quality/climate models”.

114 Another gap emerges when studying wildland fires using observations. In the past
115 decades, a number of field campaigns have revealed remarkable insights into the physical and
116 chemical processes in wildland fire plumes. For logistic and safety reasons, the early stage of the
117 plume (e.g., first hour or younger) remains poorly sampled. Controlled laboratory experiments

118 enable detailed characterizations of the fuel and the initial smoke (e.g., Hodshire et al., 2019a;
119 Roberts et al., 2020), however, these laboratory studies also only provide limited information on
120 the chemical evolution in the early stages of a wildfire plume. The early stage of the fire plume
121 (e.g., first hour or so) often involves plume rise and dilution, as well as rapid changes in
122 microphysical properties (Hodshire et al., 2019b; Konovalov et al., 2019; Schwarz et al., 2008).
123 The early stage of fire plumes remains poorly studied and a better understanding is needed.

124 Numerical models are a valuable tool to understand the chemical evolution in wildland
125 fire plumes. For instance, Lagrangian models have been used to track the plume-scale chemical
126 evolution (e.g., Alvarado et al., 2015; Alvarado & Prinn, 2009; Coggon et al., 2019; Hodshire et al.,
127 2019; Mason et al., 2006; Trentmann et al., 2005), and have greatly advanced our understanding
128 of chemical transformation and gas-aerosol interactions in wildfire plumes. However, such
129 models are not designed to resolve the spatial heterogeneity in wildfire plumes, which may
130 largely drive the variability in observations within wildfire plumes. In light of this, high resolution
131 Eulerian type plume models have been used to study the chemical evolution in wildfire plumes
132 (Alvarado et al., 2009; Trentmann et al., 2002; Trentmann et al., 2003). In particular, Trentmann
133 et al. (2003) revealed remarkable chemical heterogeneity within the fire plume, with OH radical
134 enhanced in the edges of the plume, and O_3 suppressed in the early stage of the plume but
135 enhanced in the later stage (Trentmann et al., 2003). Similar spatial heterogeneity in OH and O_3
136 has been inferred for power plant plumes as well (Brock et al., 2002). However, such Eulerian
137 type plume models are often computationally demanding, posing a limit to the spatial resolution
138 and/or the domain size, both of which affect the capability of capturing turbulent processes
139 (Agee & Gluhovsky, 1999; Roode et al., 2004). Moreover, the observational datasets available to

evaluate the chemical heterogeneity revealed in such Eulerian models were not readily available in previous studies.

The motivation of this work is to use a high-resolution turbulence-resolving model (large eddy simulation, LES) to study the chemical evolution in the early stages of a wildland fire plume, and evaluate the results using airborne observations. The LES model within the Weather Research and Forecasting (WRF) package (Moeng et al., 2007) is coupled to a simple yet representative chemical mechanism. The plume dynamics and interactions with the flow field are resolved; the fire source characteristics, terrain, and variations in the meteorology, are highly idealized, allowing to focus on the chemical evolution. The modeling experiment in this work is configured for the Williams Flats Fire (47.9392^{o}N, 118.6183^{o}W), a large wildfire ignited on 2 August 2019 in the State of Washington, U.S. This fire was extensively sampled by a number of research aircraft and satellites during the Fire Influence on Regional to Global Environments and Air Quality (FIREX-AQ) field campaign (July-September 2019). FIREX-AQ was a comprehensive airborne mission jointly funded by National Oceanic and Atmospheric Administration (NOAA) and National Aeronautics and Space Administration (NASA), focusing on the trace gases and aerosols emitted from wildfires and their impacts on air quality and climate in the United States. Airborne measurements collected from the NASA DC-8 aircraft are used to evaluate the chemical heterogeneity predicted by the model.

2. WRF-LES-CHEMISTRY MODEL

In this work, the LES model in the WRF package (version 4.0) is run in an idealized configuration, with a domain size of 70 km × 30 km × 6 km. The horizontal grid resolution is 100

m, and the vertical resolution is ~78 m near the surface and up to 138 m near the top of the model. The total number of grid boxes is 126,000,000, and the time step is 1 second. More details of the LES model configuration are provided in the Supporting Information (Section S1). This LES model is coupled with a simple yet representative chemical mechanism, consisting of 39 transported tracers and 69 reactions, covering major tropospheric chemical reactions involving key NO_x/VOC/O_3 chemistry (Table S1). This chemical mechanism is condensed based on the widely used MOZART T1 mechanism in the WRF package (Knote et al., 2014). Photolysis frequencies are calculated using the Fast Tropospheric Ultraviolet-Visible scheme (Tie et al., 2003). Two inert aerosol tracers, black carbon (BC) and organic carbon (OC), are included in this mechanism, to account for the aerosol impacts on radiation and chemistry, via both photolysis frequencies and heterogeneous chemistry. The LES model is initialized using the vertical soundings (potential temperature, water vapor, and wind) and vertical profiles of chemical species from a mesoscale WRF-Chem simulation for the Williams Flats fire. More details of this mesoscale WRF-Chem simulation are given in the Supporting Information (Section S2, Figures S1 and S2). The LES model is spun-up for two hours (from 20:00:00 to 22:00:00 3 August 2019, all times are in UTC unless otherwise noted. UTC = Coordinated Universal Time) and simulated for three more hours (22:00:00 3 August 2019 to 01:00:00 4 August 2019). The fire plume in this LES model is driven by surface fluxes of sensible heat and chemicals, characterized based on measurements: the fire size is 0.66 km^2 and the sensible heat flux is 10^4 W/m^2, both approximated from the GOES-16 fire detection product (Li et al., 2020) for the Williams Flats Fire. The emission fluxes of chemical species are adjusted until a reasonable agreement between the modeling results and the airborne measurements is reached (Section 3). The adjusted emission

fluxes are given in Table S2. This LES configuration does not have terrain, posing another limitation to the capability of resolving the observed plume transport and dispersion.

3. AIRBORNE OBSERVATIONS USED FOR MODEL EVALUATION

On 3 August 2019, the DC-8 aircraft sampled the Williams Flats fire plume in two flight patterns (Figure 1): Firstly, an overpass (bird's eye view) above the plume from 21:45 UTC to 21:59 UTC (3 August 2019) over the plume provides the structure of the plume along the direction of the spread of the fire plume using the downward-looking NASA Langley Airborne Differential Absorption Lidar (DIAL). Secondly, the aircraft descended and flew through the plume in a "lawnmower" pattern, providing a number of semi-Lagrangian transects. The one second merge dataset provided by the NASA Langley Research Center is used in this work, including high time response measurements from a number of instruments, except for the NCAR Trace Organic Gas Analyzer (TOGA) with a time resolution of ~105 seconds (with a sampling window of ~32 seconds). Table S3 summarizes all measurements used in this work.

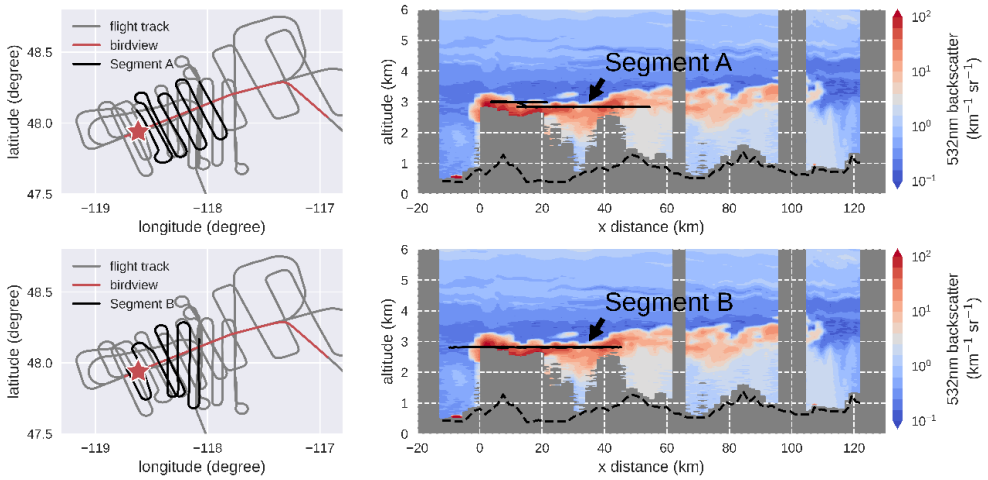

Figure 1. (Left) Flight tracks and (right) 532 nm backscatter ratio measured using NASA DIAL. The flight altitudes during Segments A and B (solid black lines in the Right panel) are overlaid on top

of the "bird's eye view" curtain in the Right panel, but Segments A and B occurred at different times than the "bird's eye view" flight.

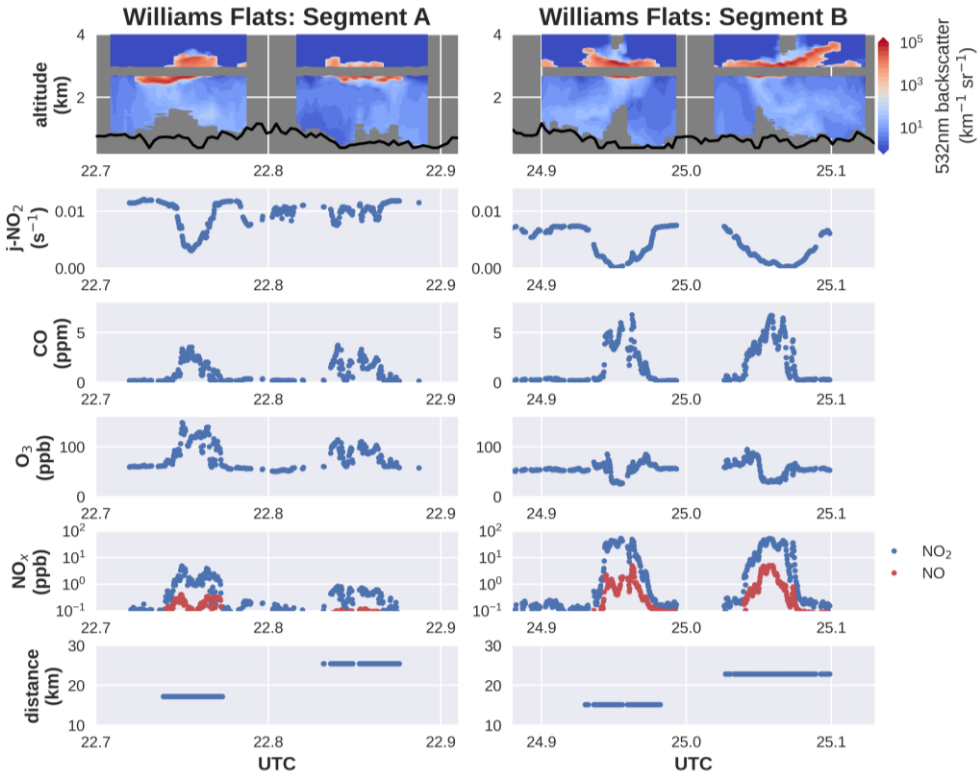

Figure 2. Selected airborne measurements collected during the "in-plume" Segments A and B, two transects each. The full view of Segments A and Segments B is provided in Figure S3.

The second stage (semi-Lagrangian transects) consists of two major segments: Segment A, from 22:20-23:15 UTC (3 August 2019), and Segment B, from 00:30-01:24 UTC (4 August 2019). Segments A and B both sampled the first ~50 km of the plume, however, there are several marked differences: (i) The GOES satellite image suggests that, before the DC-8 aircraft sampling, the Williams Flats Fire region was dominated by a north wind in the boundary layer, transporting the Williams Flats fire towards the south. Starting from ~17:00 UTC the low-level wind direction shifted to the west-southwest, transporting the smoke to the east-northest. Therefore Segment A sampled some aged/diffused smoke (due to the shift in wind direction), while the smoke sampled during Segment B was relatively well defined "fresh" smoke. (ii) Based on the

combination of remote sensing and *in situ* measurements, the DC-8 aircraft likely flew through the dense "core" of the plume during Segment B, while Segment A likely skimmed the upper edge of the plume. During Segment B, the sampled plume was rather optically opaque such that the DIAL laser signal was severely attenuated at the center of each transect (Figure 2). Accordingly, the measured photolysis frequencies, such as j-NO_2, were suppressed at the center of each transect (Figure 2). O_3 was also suppressed at the center of the plume due to the rapid reaction with NO (Figure 2). During Segment A, however, measured CO and NO_x levels inside the plume were lower than that during Segment B, and the j-NO_2 reduction inside the plume was also weaker than that during Segment B (Figure 2), implying that the Segment A perhaps mostly sampled the upper part of the plume, which is optically thinner and with lower levels of primary pollutants. Interestingly, O_3 during Segment A was always enhanced at the center of each transect (Figure 2), similar to the O_3 measured when the DC-8 aircraft was entering and leaving the plume in Segment B (i.e., the edges of the plume sampled in Segment B), providing additional evidence that the aircraft sampled the top part of the plume during Segment A. The modified combustion efficiency, defined as $\Delta CO_2/(\Delta CO+\Delta CO_2)$ (Yokelson et al., 2008), did not vary dramatically between the two Segments (both 0.89-0.92), implying the average burning condition remained relatively consistent during these two Segments. To sum up, the DC-8 measurements during Segment A may not reflect the center of the plume, and thus Segment B is mainly used for model evaluation.

A variety of merged files have been created for each research flight. In this work, the 1-Hz merge files are used unless otherwise noted. More details of the merging algorithm can be found elsewhere (https://www-air.larc.nasa.gov/missions/etc/onlinemergedoc.pdf).

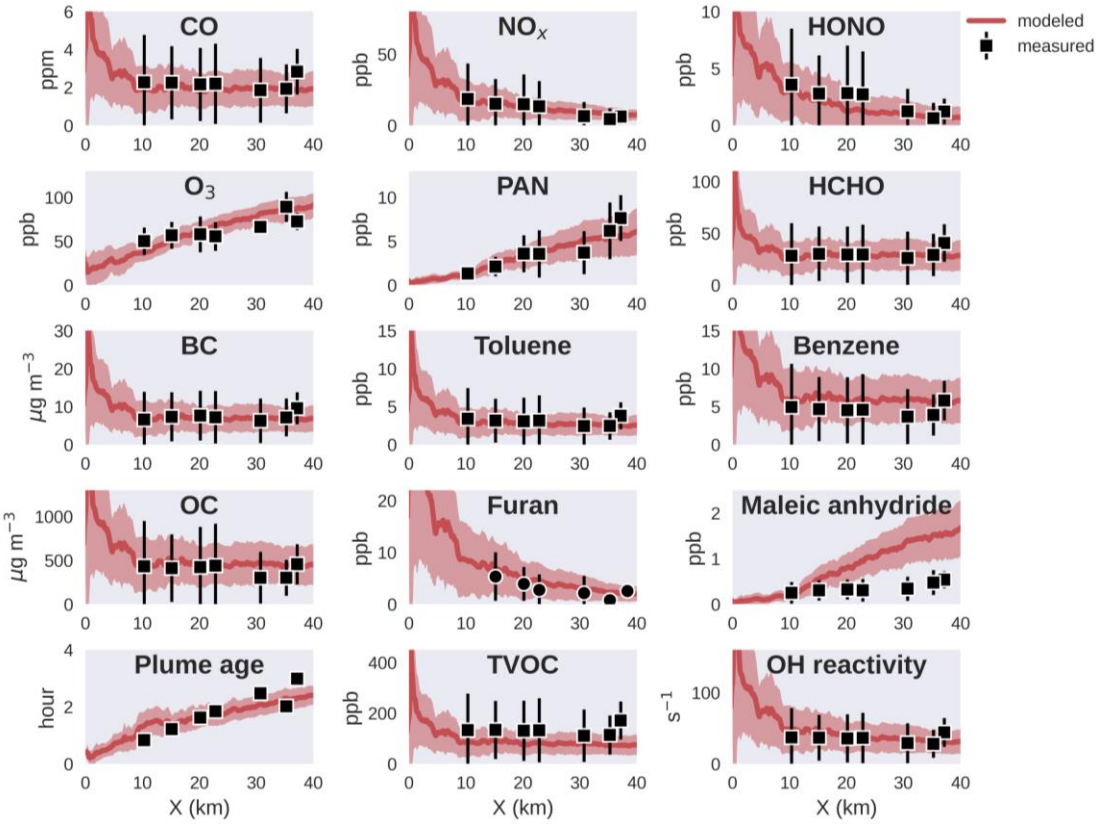

Figure 3. Modeled plume-wide averages and standard deviations (red lines and shadings) of selected compounds and parameters, compared to the airborne measurements averages and standard deviations (black symbols and error bars) during each transect during Segment B at X km downwind. The measurements are averaged using the smoke flag provided in the 1-Hz merge, while the modeled plume-wide averages are calculated for each plume cross section at X km downwind. OC is calculated from organic aerosol and OA/OC ratio measured using the CU HR-AMS. The measurement-derived plume age is estimated from the measured winds and distance from the fire location (provided in the 1-Hz merge), while the plume age in the model is estimated based on Equation 1. Total measured volatile organic compounds (TVOCs) are listed in the main text and Table S3. Total OH reactivity is calculated for TVOCs as well as CO and methane.

Figure 3 compares the model chemical species and parameters to the airborne observations collected during Segment B, providing a semi-quantitative comparison of the plume chemical evolution as a function of distance in km from the fire source (X). As shown, the model captures the chemical characteristics within the plume reasonably well, as the modeled plume-wide means of gaseous (CO, NO_x, HONO, HCHO, O_3, and PAN) and aerosol constituents (BC and

OC) are both in good agreement with observations, although the observations do show larger variations than the modeled. Total VOCs were calculated as the sum of the mixing ratios of ethane, propane, i-butane, n-butane, i-pentane, n-pentane, i-butene + 1-butene, isoprene, MVK, MACR, benzene, toluene, formaldehyde, acetaldehyde, methanol, ethanol, acrolein, acetone + propanal, furan, 2-methylfuran + 3-methylfuran, furfural, phenol, and styrene, reported from several different instruments on board the DC-8 (Table S3). Notably, the simplified mechanism captures roughly about half of the measured total VOCs, yet the modeled total OH reactivity is comparable to the calculated total OH reactivity based on measurements available (Figure 3).

In the model, two fire tracers are added to track the physical age of any air parcel in the plume: one tracer with 1-hour fixed lifetime, and the other inert one with infinite lifetime. The plume physical age (in hours) is given by:

$$Physical\ age = -\ln\left[\frac{Tracer\ 1\ (\tau=1\ hr)}{Tracer\ 2\ (\tau=\infty)}\right] \qquad \text{Equation 1}$$

As shown in Figure 3, the modeled physical age also shows good agreement with that estimated using airborne measurements (estimated from measured winds and distance from center of transect to the fire source), implying that the meteorological conditions (especially wind) are decently represented in this simple model configuration. The total OH reactivity in the model (including CO and methane) is also in reasonable agreement with the total OH reactivity calculated using airborne measurements, despite the fact that the chemical mechanism used in this model is highly condensed. Overall, this figure reveals that the highly simplified model configuration and chemical mechanism captures the major chemical characteristics of the plume. We discuss the detailed plume physics and chemistry in the following sections.

4. PLUME DYNAMICS IN THE EARLY STAGE OF THE PLUME

The high-resolution LES model resolves the turbulence induced by the fire source and the interactions with the background flow field. Due to the strong heat release from the fire, the plume rapidly rises in the early stage, characterized by high updraft speed in the early stage (modeled mean updraft: 3 m s^{-1} in Figure 4; maximum updraft in the model reaches up to 12 m s^{-1}). The strong updraft injects the plume into a lofted layer that is 1.5-2.5 km above the surface, consistent with the DIAL measurements (~1.5-3 km above ground level, Figures 1 & 2). The rapid updraft at the center of the plume leads to downdraft and hence small circulations near the plume, as indicated by the streamlines in the cross section plots (Figure 4). The rapid plume rise and the circulations also lead to dilution. In the model, the plume 1st order dilution rate can be quantified by tracking the decay of the inert fire tracer:

$$Dilution\ rate\ (s^{-1}) = \frac{dln([Tracer\ 2])}{dt} \qquad \text{Equation 2}$$

Where *[Tracer 2]* is the concentration of the inert fire tracer and *t* is the plume physical age. As shown in Figure 4, the plume dilution rate is on the order of 0.001 s^{-1} in the early stage of the plume, which is decreased to and maintained at the order of 0.0001 s^{-1} in the late stage of the plume. The plume dilution leads to entrainment of the background air.

Different processes drive the plume dilution. In the uprising stage (e.g., X = 1 km), the dilution is mostly driven by the circulations induced by the plume-rise, therefore faster at the bottom of the plume, where the entrainment flows enter the plume. Later on, the plume rise has ceased (e.g., X = 10 and 30 km, with mean vertical velocity (w) close to zero), the plume-wide mean dilution is nearly an order of magnitude slower than that in the uprising stage, and is still faster at the edges of the plume.

299 Notably, the model predicts the lower part of the plume may be strongly mixed
300 throughout the boundary layer, due to the convective mixing within the boundary layer. As a
301 result, the horizontal dispersion in the lower part of the plume is slower, compared to the upper
302 part (Figure 4). This is typical for daytime wildland fire plumes with low-intermediate plume
303 injection, which is also consistent with the DIAL images that diffused smoke extends from right
304 below the dense smoke all the way to the surface (Figures 1 & 2).

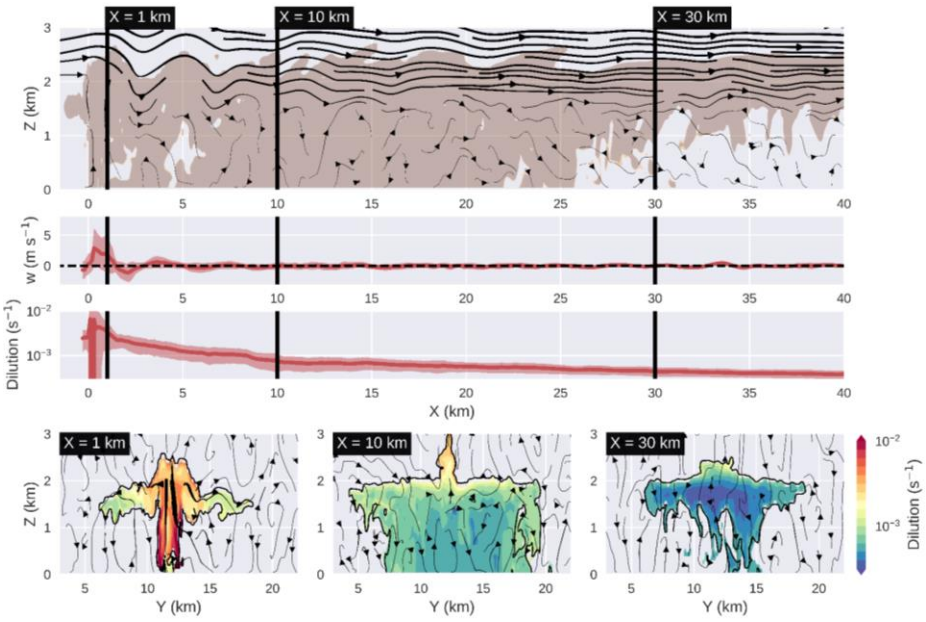

305

306 Figure 4. (Top) Streamlines at the centerline of the plume (curtain); (middle) plume-wide average
307 updraft speed and dilution rate (shadings: standard deviations); (bottom) dilution rate cross
308 section at X = 1, 10, and 30 km. The thickness of the streamlines roughly represents the wind
309 speed. The vertical black lines represent the locations of the cross sections. The plume (brown
310 colored area) is defined as CO > 150 ppb.
311

312 **5. PHYSICAL AND CHEMICAL EVOLUTION IN THE EARLY STAGE OF THE PLUME**

313 The LES configuration coupled with chemistry reveals how the plume evolves over the
314 course of dispersion. Figure 5 briefly shows how the plume ages physically, and also provides an
315 overview of the chemical evolution in fresh plume via two important reactive species: OH radicals

for photochemistry, and NO_3 radicals for dark chemistry. The physical age shows considerable heterogeneity vertically - the lower part of the plume is generally older than the upper part of the plume (Figure 5), which is a combined result of the vertical wind gradient, and enhanced mixing within the boundary layer.

OH radicals are the major driver of atmospheric oxidation. The model predicts very interesting heterogeneity within the fire plume: in the early stage of the plume (first ~8 km or so), OH is severely suppressed in the bulk of the plume, but enhanced at the upper most edge of the plume (Figure 5). This is mainly because the solar radiation is severely attenuated in the plume due to the presence of high levels of aerosols. Further downwind, OH radicals become enhanced in the upper part of the plume (~8-30 km), or even the entire vertical extent of the plume in the later stage (~30+ km, Figure 5). NO_3 radical, a major oxidant in the atmosphere under dark conditions, is also present in the modeled plume at the same time, but only in the lower-most part of the plume and, to a lesser extent, below the thick plume (Figure 5). In particular, the modeled NO_3 mixing ratio reached ~3 ppt in the lower-most part of the plume in the early stage. With the dilution and entrainment, the NO_3 oxidation products in the lower-most part of the plume or below the plume may be mixed into the bulk of the plume. A recent study reported rapid aging of biomass burning aerosols under dark conditions (driven by NO_3 radical), a potential source of organic aerosols that has not been widely considered (Kodros et al., 2020). The chemical heterogeneity within fresh wildland fire plumes warrants further investigation.

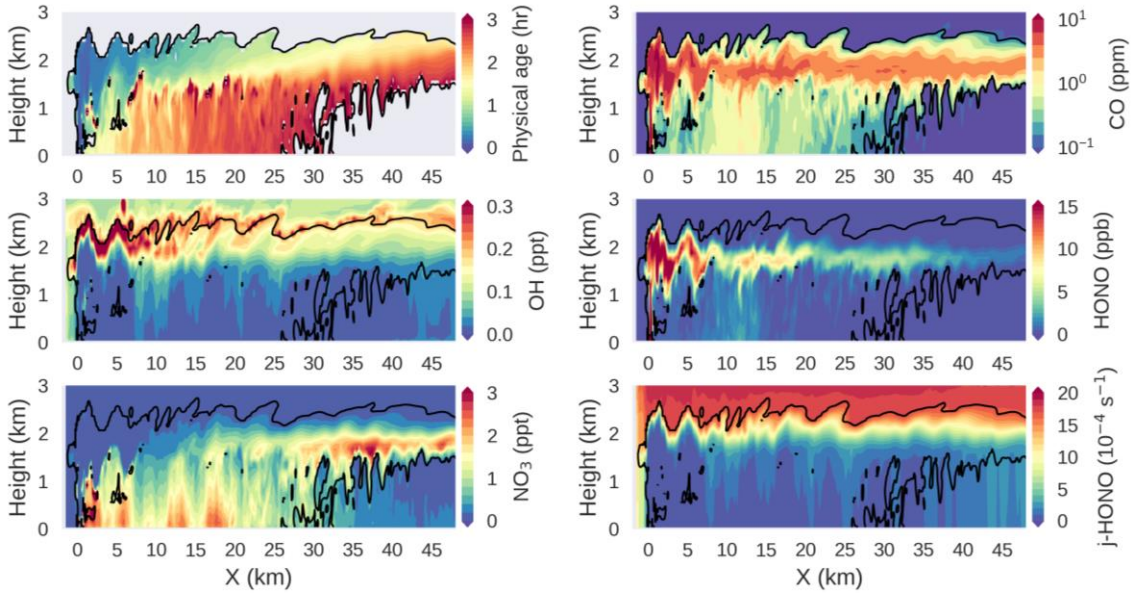

Figure 5. Modeled curtains of the plume physical age and mixing ratios of OH, NO_3, CO, HONO, and the photolysis frequency of HONO (j-HONO). The curtains are at the centerline of the plume. The black lines represent the roughly defined the plume boundary (CO = 150 ppb)

6. CHEMICAL TOMOGRAPHY IN THE PLUME

In this section, we discuss the modeled chemical tomography inside the plume, as well as the observational evidence. We focus on the cross-transect variations of a few species: CO, O_3, PAN, maleic anhydride (a product from furan oxidation), and HONO. Again because of the difficulties in providing realistic initial and boundary conditions to the LES model, also the fact that this simplified LES configuration does not consider terrain impact, it is unrealistic to compare the modeling outputs to the DC-8 measurements precisely. Therefore, the modeled fields are not sampled along the flighttrack. Instead, the comparison is focusing on whether the model is capable of reproducing the broad features in the observations. In this section, several aircraft transects showing distinct cross-transect variations are selected, and compared to cross sections of the modeled plume sampled at the same downwind distances at 2 km above the model surface (aircraft altitude: ~2.8 km during Segment B, mean terrain height 0.85 ± 0.32 km).

Figure 6 shows the observed cross-transect variability of CO, a (mostly) primarily emitted fire tracer with fairly long atmospheric lifetime. As shown, the observed CO is generally elevated at the center of the plume, except at X = 30 km the observed CO shows two distinct "modes", possibly due to the influence of very aged/diffused smoke. The modeled cross sections at the same transect distances show very good agreement with observations at X = 5-15 km. At X = 30 km, the model is able to capture one of the "modes". Because of the simple model configuration (e.g., short simulation time, small domain, no smoke in the boundary condition), it is challenging for this model to capture aged/diffused smoke. Overall, Figure 6 demonstrates that the model captures the plume dispersion and transport quite well (at least in the first ~15 km).

Similar cross-transect variations for j-HONO, NO_x, HCHO, BC, and OC are provided in the Supporting Information. In general, the model well captures the cross-transect variations of these constituents in the first ~15 km (Figure S4-S8), and they are all enhanced inside the plume relative to that at the edges. The model captures j-HONO outside the plume but overestimates j-HONO inside the plume by ~20% (relative to the background j-HONO, Figure S4). In addition, the *in situ* measurements show that plume "optical width" (the plume width characterized by the measured j-values) appears to be wider than the plume "chemical width" (the plume width characterized by the chemical constituents). Although the modeled plume "chemical width" is generally well captured by the model in the first ~15 km (Figures 6, S4-S8), the plume "optical width" is underestimated by the model (Figure S3). The model underestimation of j-value suppression inside the plume and the underestimation of the plume "optical width" may be due to the 3-D radiation effect (Trentmann, et al., 2003) that is not captured by FTUV (Tie et al., 2003), although we cannot rule out the possibility of diffused or high level smoke/cloud not captured in the model.

374 Moreover, only BC and OC are considered in this work. Although CU HR-AMS measurements
375 suggest that organic aerosols alone accounts for 93% of measured PM_1 mass, recent studies
376 found that brown carbon may also contribute to light absorption in biomass burning plumes
377 (Palm et al., 2020). In summary, primarily fire-emitted long-lived tracers such as CO, BC show
378 Gaussian-like cross-transect profiles. In the next few sections we will examine a few compounds
379 with drastically different cross-transect profiles

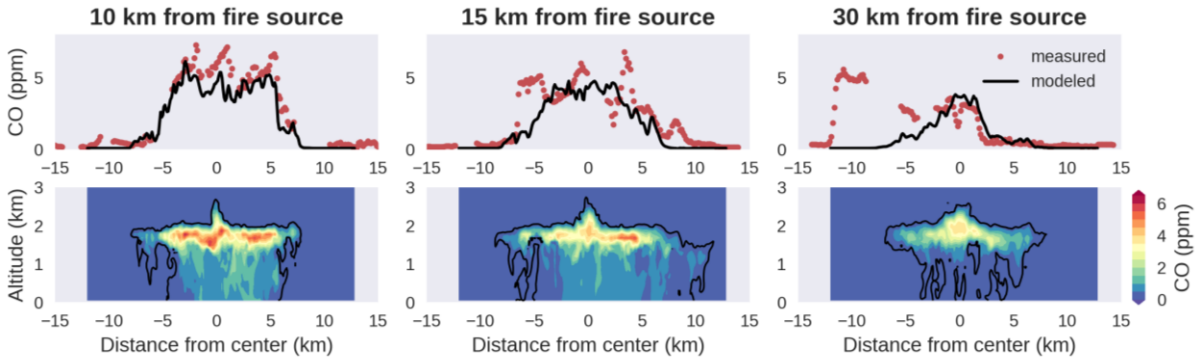

380

381 Figure 6. Measured CO (top) during Segment B and modeled O_3 cross sections (bottom) at 10 km,
382 15 km, and 30 km downwind of the fire source. Also shown in the top panel are the modeled CO
383 sampled at the same distance from the fire, at ~2 km above the model surface.
384

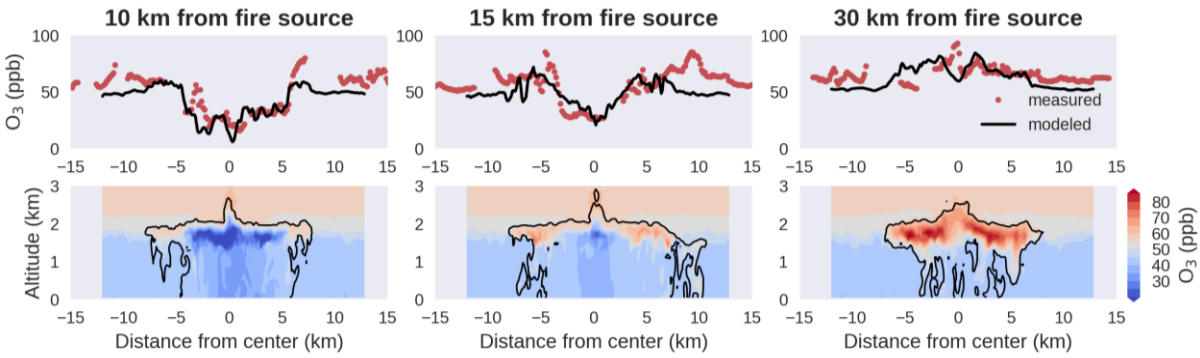

385

386 Figure 7. Measured O_3 (top) during Segment B and modeled O_3 cross sections (bottom) at 10 km,
387 15 km, and 30 km downwind of the fire source. Also shown in the top panel are the modeled O_3
388 sampled at the same distance from the fire, at ~2 km above the model surface.
389

6.1. CROSS-TRANSECT VARIATION OF OZONE

As shown in Figure 7, O_3 shows considerable heterogeneity within the modeled plume. In the early stage (X = 10 km), the model predicts that O_3 is suppressed inside the plume (up to 30 ppb lower than the background O_3 at the same height), because of fire-emitted NO. Normally, NO_2 produced from NO-O_3 reaction would undergo photolysis and produce O_3 back; but j-NO_2 is strongly suppressed within thick fire plumes, and NO_2 will not photolyze and hence serves as a temporary reservoir for O_3. The modeled O_3 during this transect compares well to the measurements. At X = 15 km, measured O_3 is recovered at the center of the transect and is elevated at the edges, and the model shows similar broad features. At X = 30 km, the measured O_3 is well mixed throughout the plume, and is enhanced relative to the background by 10-40 ppb. The model predicts a consistent O_3 trend at X = 30 km that O_3 is enhanced throughout the plume, compared to the background air.

As discussed in Section 3, Segment B is used to examine the cross-transect variations of O_3, since the aircraft flew through the core of the plume multiple times during Segment B. However, the edge effect on O_3 is also visible in Segment A, when the aircraft likely sampled the upper edge of the plume. The measured O_3 is enhanced relative to the background in all transects during Segment A (Figure 2) by up to 100 ppb, roughly 2 times greater than the O_3 sampled at the edges of the plume during Segment B. This may indicate possibly stronger O_3 enhancement at the upper edge of the plume than the sides of the plume. The model also shows enhanced O_3 levels at the upper edge of the plume (Figure 7) relative to the sides of the plume, but the magnitude of the O_3 enhancement is again underestimated by the model.

411 Overall, the model qualitatively captures the observed O_3 variations in these transects,
412 but seems to underestimate the O_3 enhancement at the edges. The plume-wide average of
413 O_3+NO_2 reaches ~40 ppb higher than that in the background air after ~2 hours of aging, indicating
414 net O_3 formation in this modeled plume. Note that in previous studies, O_3 is not always found to
415 be enhanced relative to the background air especially in more aged (e.g., a few days or older)
416 biomass burning plumes (Alvarado et al., 2010; Parrington et al., 2013). Because of the highly
417 simplified VOC chemistry used in this model, we do not intend to further investigate O_3 formation
418 and variability, which is beyond the scope of this study. But we show that the observed cross-
419 transect variations in O_3 can be qualitatively explained by including simple chemistry with a
420 turbulence-resolving model.

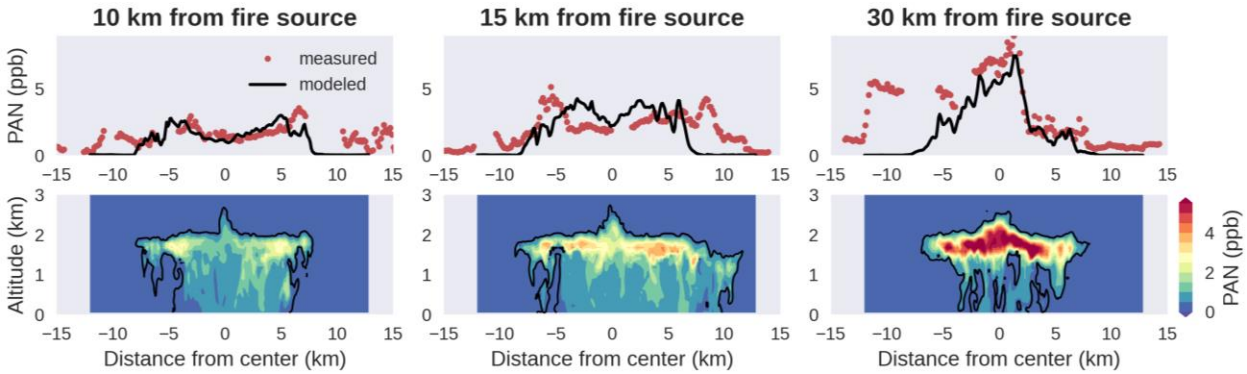

421

422 Figure 8. Measured PAN (top) during Segment B and modeled PAN cross sections (bottom) at 10
423 km, 15 km, and 30 km downwind of the fire source. Also shown in the top panel are the modeled
424 PAN sampled at the same distance away from the fire, at ~2 km above the model surface.
425

426 **6.2. ELEVATED PAN LEVELS AT THE PLUME EDGES**

427 PAN is an important reservoir of NO_x. Previous studies have reported rapid PAN formation
428 in biomass burning plumes (Alvarado et al., 2010, 2015; Fischer et al., 2018; Jaffe et al., 2013; Liu
429 et al., 2017; Singh et al., 2012). Because of the limited capability in resolving the transport and

chemistry of reactive nitrogen species in early biomass burning plumes, large scale models sometimes partition a fraction of the reactive nitrogen emissions as PAN (Fischer et al., 2014), and this process is subject to potential uncertainties because of non-linear dependency of PAN formation on VOCs and NO_x (somewhat similar to O_3). In this section, we examine PAN formation in the modeled fresh plume as the plume ages.

As shown in Figure 3, the modeled plume-wide mean PAN is in reasonable agreement with observations. Figure 8 shows the cross-transect comparison for PAN. Interestingly, at X = 10 and 15 km, measured PAN is elevated at the edges of the plume compared to that at the center. In particular, at X = 15 km, the measured PAN is nearly doubled at the edges. The model reproduces this feature at X = 15 km but tends to overestimate PAN by 2-3 ppt. The edge enhancement of PAN occurs because in the early stage of the plume, PAN formation is limited by the initial OH attack on its VOC precursors, and OH production is more active at the edges of the plume. At X = 30 km, however, it appears that the measured PAN is spread out in a wider range than the model predicts, similar to a few other compounds (Figures 6 & S5-S8). Overall, PAN formation accounts for 10-70% of the NO_x loss in this modeled plume. In summary, the observed PAN shows interesting core-edge differences in the early stage of the plume, corroborating faster photochemical aging at the edges of the plume. This effect may be largely diminished in the later stages of the plume, because dilution further lowers the aerosol loading inside the plume, and hence the suppression of photochemistry inside the plume becomes weaker. Notably, elevated PAN is often found outside the studied plume (i.e., other pollutants such as CO are close to the background levels), providing additional evidence of possible diffused/aged smoke.

6.3. FURANS AS A FIRE-TRACER AND INDICATOR OF PHOTOCHEMICAL AGING

Furans are an important VOC class emitted from biomass burning, contributing substantially to the total VOC reactivity in biomass burning plumes (Coggon et al., 2019). In this section, we discuss the simplified furan chemical mechanism included in the LES model (Table S1), as well as the photochemical aging tracked by furan and one of its unique oxidation products, maleic anhydride. For simplicity, "furan" in this model is a lumped species representing total furan species, and the modeled furan is compared to the TOGA measurements (sum of furan, 2-methlyfuran, 3-methlyfuran, and furfural). We do not compare the modeled furans to the PTR-MS measurements during Segment B since secondary products and lesser-reactive isomers likely result in measurement biases after several hours of oxidation (Coggon et al., 2019; Koss et al., 2018).

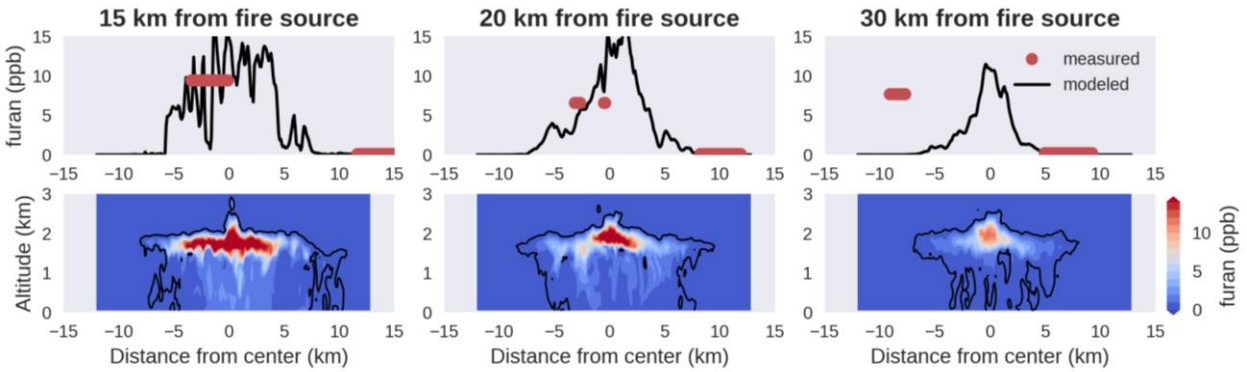

Figure 9. TOGA measured total furans (top) during Segment B and modeled furan cross sections (bottom) at 15 km, 20 km, and 30 km downwind of the fire source. Also shown in the top panel are the modeled furan sampled at the same distance from the fire, at ~2 km above the model surface.

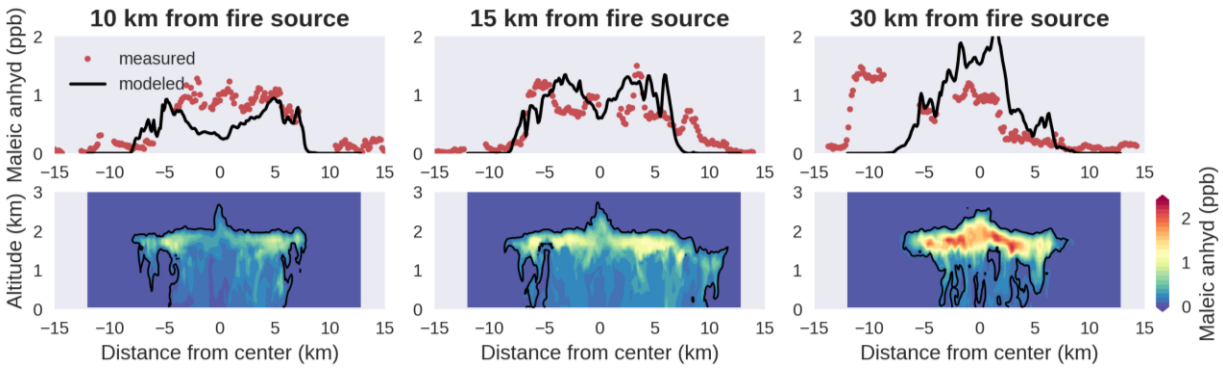

Figure 10. PTR-MS measured maleic anhydride (top) during Segment B and modeled maleic anhydride cross sections (bottom) at 10 km, 15 km, and 30 km downwind of the fire source. Also shown in the top panel are the modeled maleic anhydride sampled at the same distance from the fire, at ~2 km above the model surface.

Furans are primarily emitted from fire, and their major sink is the reaction with OH radicals, and to a lesser extent, with O_3 and NO_3 (Coggon et al., 2019). Figure 9 shows the measured and modeled furans. As shown, the modeled and measured furan show reasonable agreement at X = 15 and 20 km, but not at 30 km. The modeled cross-transect variability of furan at X = 15 is similar to other primary compounds such as CO (Figure 6), i.e., concentrated at the center/core of the plume but reduced at the edges. Its oxidation product, maleic anhydride, however, is enhanced at the edges according to the measurements at X = 15 km. Such core-edge discrepancy is consistent with PAN (Section 6.2), and also implies faster photochemical aging at the plume edges. This core-edge discrepancy at X = 15 km is qualitatively captured by the model (Figure 10). At X = 10 km, the model also predicts similar core-edge discrepancy. The measured maleic anhydride at X = 10 km, however, shows a peak at the center of the transect in addition to the two peaks at the edges. This might imply that perhaps a small fraction of maleic anhydride may be directly emitted from the fire source. Maleic anhydride emissions have not been reported in the literature, but a reanalysis of measurements conducted during the FIREX Firelab 2016 study

(Coggon et al., 2019; Koss et al., 2018) shows that PTR-MS measurements of maleic anhydride represent 1-2% of furan emissions, suggesting that emissions likely contribute to higher plume center mixing ratios at X = 10 km.

The impact of plume chemical heterogeneity on furan decay is also examined using the modeling results. We discussed in Section 5 and Section 6.1 that ozonolysis and NO_3 oxidation may be active in optically dense smoke, and furan can be oxidized by O_3, and NO_3 as well. We found that OH oxidation is the dominant furan loss pathway, accounting for 78-89% of total furan loss. Ozonolysis and NO_3 oxidation account for up to 16% and 7% of total furan loss, respectively. The relative importance of the three oxidation pathways evolves with time: OH oxidation accounts for >90% in the early stage, while ozonolysis and NO_3 oxidation together contribute to <10% furan oxidation in the early stage. Further downwind, with the gradual recovery of O_3, the contribution of ozonolysis increases to up to ~30% at X = ~30 km, where NO_3 oxidation also contributes to another ~20% of total furan loss. NO_3 oxidation mostly occur in the lower part of the plume, while furan mostly exists in the bulk of the plume aloft. Therefore, the NO_3 oxidation is partially affected by the plume dynamics. The impact of chemical heterogeneity on the overall VOC reactivity is challenging to represent in small-scale Lagrangian type models or large-scale models with coarser spatial resolutions.

6.4. HONO: SECONDARY PRODUCTION, IMPACT OF PLUME DYNAMICS

HONO is an important precursor of OH radicals in the atmosphere and is emitted from wildland fires (Peng et al., 2020; Theys et al., 2020). In this modeling work, we include both primary HONO emission and secondary HONO formation from NO_2 heterogeneous reaction on

512 BC and OC aerosols (both reasonably well captured by the model, Figures S7-S8). The reactive
513 uptake coefficient of NO_2 is mostly on the order of 10^{-5}-10^{-4} in the literature (Ammann et al.,
514 2013). Therefore, we assume the NO_2 uptake coefficient on aerosols is 5×10^{-5} in this work. Model
515 sensitivity tests are also performed to examine the possible secondary HONO production. As for
516 the primary HONO emission, it depends on the fuel type, which is primarily grassland with tall
517 grass, timber, and brush in this region (https://inciweb.nwcg.gov/), and the average HONO/NO
518 emission ratio (molar basis) for savannah/grassland and temperate forest are 12% and 7%,
519 respectively (Andreae, 2019). This is consistent with a recent laboratory study in which HONO
520 accounts for 13% of NO produced from stack fires (Roberts et al., 2020). In this work, we found a
521 fire HONO emission of 11% of fire NO emission (molar basis) yields the best agreement when
522 compared to airborne HONO measurements (Figure 3): modeled plume-wide mean HONO
523 exceeded 10 ppb in the very beginning stage of the plume, which then decreased to 2-4 ppb at
524 10-25 km downwind, and eventually to 1-2 ppb at 30-40 km downwind.

525 Figure 11 shows the cross transect comparison for HONO. As shown, the measurements
526 suggest that HONO is concentrated at the center of the plume, and the modeled HONO levels
527 across the transects show good agreement with observations, especially in the early stage (X =
528 10 and 15 km). The model also shows that HONO is always depleted at the edges, especially the
529 upper edge of the plume (Figure 11). The cross transect comparison for HONO/NO_2 ratio is given
530 in Figure S10. This ratio remains fairly constant at the center of the modeled plume (with
531 secondary HONO production), but rapidly decreases at the edges of the plume. At X = 30 km
532 downwind, the model drastically overestimates HONO, mainly due to the overestimation in NO_x
533 (Figure S5). This is likely because the sink of NO_x is not well captured by this highly condensed

534 chemical mechanism. Notably, we discussed previously that the model fails to predict the plume
535 profile at X = 30 km, since the observations show two distinct "modes" at X = 30 km and model
536 captures only one of them (Figures 6, 8, 10, S5-S8). Figures 11 and S5 show that the observed
537 HONO and NO_x are higher in the other "mode", consistent with the modeled HONO and NO_x,
538 respectively. This may also imply a change in meteorological condition which alters the plume
539 transport that is not captured by the simple model configuration.

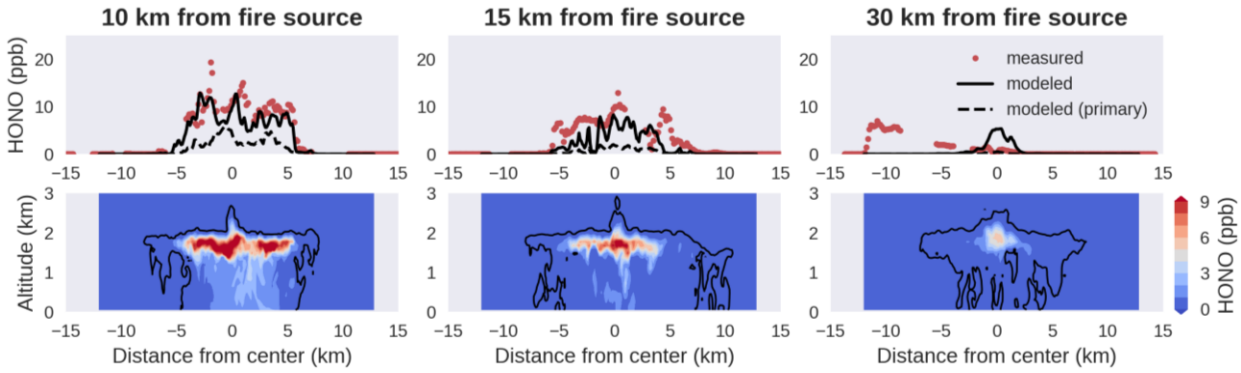

540

541 Figure 11. Measured HONO (top) during Segment B and modeled HONO cross sections (bottom)
542 at 10 km, 15 km, and 30 km downwind of the fire source. Also shown in the top panel are the
543 modeled HONO sampled at the same distance away from the fire (solid black line: with secondary
544 HONO production from NO_2 heterogeneous reaction; dashed black line: with only primary HONO).
545

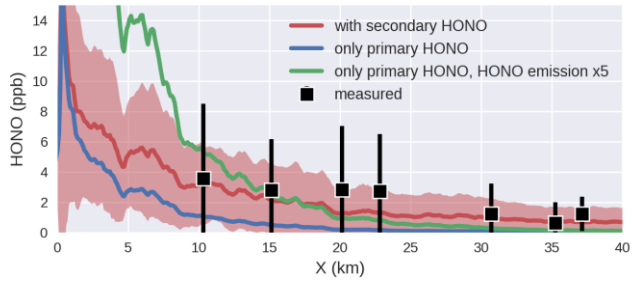

546
547 Figure 12. Measured plume-wide averages of HONO compared to modeled in different model
548 scenarios: with both primary and secondary HONO (dark red, same as that in Figure 3), with only
549 primary HONO and no secondary HONO production (blue), primary HONO emission increased by
550 a factor of 5 and no secondary HONO production (green).

551 We now discuss the potential secondary HONO production from NO_2 heterogeneous
552 reactions on aerosols in the modeled plume. As shown in Figure 11 and Figure 12, the model

553 simulation with secondary HONO production yields best agreement with observations. Without
554 secondary HONO production, in order to capture the detected HONO levels at X = 10-15 km,
555 primary HONO emission needs to be increased by a factor of ~5 (i.e., about half of NO emission),
556 which still underestimates HONO in the later stage (X > 20 km, Figure 12). The primary HONO
557 emission contributes substantially to the total HONO levels in the early stage: the modeling
558 results suggest that >93% HONO in the early stage is from primary emission, which decreases to
559 55% at 40 km downwind (observed HONO: 1.2 ± 1.1 ppb at X = 37 km, Figure 3). Note that the
560 modeled simulation with heterogeneous conversion from NO_2 to HONO may not necessarily
561 mean a considerable increase in HONO/NO_2 ratio (Figure S9). To sum up, although no direct
562 evidence can be provided in this work, our combined observational and modeling analysis does
563 suggest that a secondary HONO source better explains the observed HONO levels and variability
564 in this particular plume.

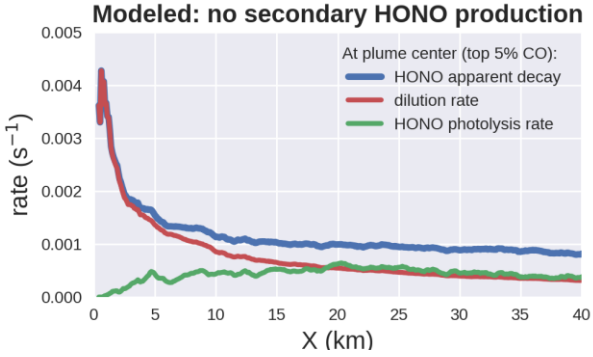

565
566 Figure 13. Modeled apparent HONO decay rate (first order) at the center of the plume, as well as
567 the modeled dilution rate and local HONO photolysis rate also at the center. This plot is created
568 using the model simulation without secondary HONO production. Plume center is defined with
569 top 5% modeled CO.

570 We now take HONO as an example to demonstrate the impact of plume dynamics on the
571 chemical evolution. We showed in Figure 4 that the modeled plume dilution (mixing) is faster in
572 the early stage (driven by strong updraft and entrainment) but is maintained relatively constant

in the later stage. The physical mixing within the plume may pose a limiting factor for slow chemical reactions. At the center of the plume, solar radiation is suppressed and hence HONO photolysis is low, leading to a local photolysis lifetime of half an hour or longer. However, as shown in Figure 13, the apparent decay rate of HONO at the center of the plume is nearly 9 times faster than the local photolysis rate, but is very close to the physical dilution rate. That is, although in the early stage photochemistry is slow in the majority of the plume, HONO still decays fairly fast – with an effective lifetime of several minutes at the dark center of the plume. The rapid mixing bring HONO from the center of the plume to the edges and upper part, where HONO is quickly destroyed via photolysis. Even at X = 40 km, physical mixing still contributes to half of apparent HONO decay at the center of the modeled plume. This exercise demonstrates the importance of plume dynamics in the chemical evolution in fresh biomass burning plumes.

HONO photolysis is the most important primary OH source in this modeled plume, while other primary OH sources (such as the photolysis of O_3 and aldehydes) are 1-2 orders of magnitude weaker (Figure S10). In addition to the primary OH sources, secondary OH sources (i.e., recycled from HO_2) also plays a key role in the simulated plume, which is on average an order of magnitude higher than the primary OH source (Figure S10), implying an efficient HO_x recycling in this modeled plume mediated by NO_x. This secondary HO_x source also efficiently propagates HO_x chemistry into the darker interior of the plume, while photons (that can trigger photochemical reactions) are quickly quenched at the edges and do not reach the bulk of optically dense plumes (e.g., Figure 5). In summary, this section highlights the importance of HONO in wildland fire plumes. The reactive uptake coefficient of NO_2 as well as the dependency on particle type and other parameters or conditions warrant further investigation.

595

596 **7. IMPLICATIONS FOR MODELS WITH COARSER HORIZONTAL RESOLUTIONS**

597 In principle, LES schemes resolve major (large) eddies, through which momentum, energy,
598 and other passive scalars are transported. This sets the upper limit of the horizontal grid size in
599 LES models to about 0.1 km. Most planetary boundary layer schemes (widely used in regional
600 and global chemical transport models) are not designed to resolve the energy-baring eddies,
601 which are parameterized as sub-grid processes instead. This sets the lower limit of the horizontal
602 grid size of most planetary boundary layer schemes to about 1 km. Moreover, operating with
603 small grid sizes (or high horizontal resolution) often also requires shorter integration time steps,
604 which also leads to an increase in computational cost. Currently, most regional chemical
605 transport models are operated at horizontal grid resolutions of a few to tens of km. In this section,
606 we discuss the impact of grid resolution on the chemical evolution of wildland fire plumes.

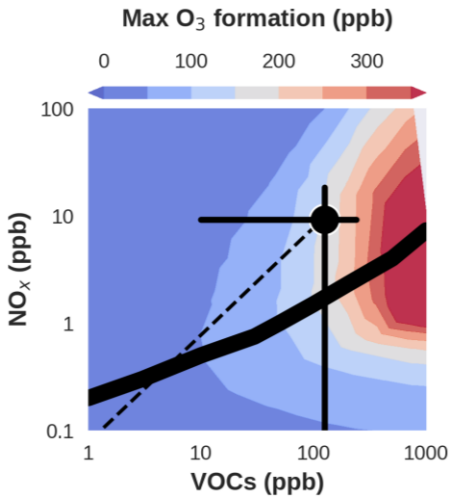

607

608 Figure 14. Sensitivities of maximum O_3 formation as a function of fire-emitted NO_x and non-
609 methane VOCs. The thick black line represents the transition between the NO_x-saturated and the
610 NO_x-limited regimes. The circle/error bars represent the airborne measurements averaged
611 during the Segment B of Williams Flats Fire (3-4 August 2019). The thin dashed line is the 1:1
612 dilution line for Williams Flats fire.
613

Biomass burning emission inventories report the emissions of pollutants on a mass basis. When using an emission inventory in a particular model, the emissions need to be re-gridded into the horizontal resolution at which the model is operated. Usually, an area weighted interpolation method would be used, since the total amount of emitted pollutants need to be conserved. If the model horizontal grid size is larger than the fire size, to maintain mass conservation, all fire emitted tracers are immediately diluted within the grid cell, leading to an instantaneous numerical dilution. For instance, the area of the fire source in this model is 0.6 km^2, and if mimicking this particular fire using a model with 4-km grid resolution (with same vertical resolution), the emission fluxes are reduced by a factor of 26.7 (4^2/0.6); if the model grid resolution is 1 km, the emission fluxes are still reduced by a factor of 1.5 (1^2/0.6). The atmospheric chemical system is highly non-linear, especially the O_3 chemistry, such that dilution may lead to a shift in chemical regimes. Figure 14 shows the sensitivity of maximum O_3 formation as a function of fire-emitted NO_x and VOCs. This plot is created using a box model with a near-explicit chemical mechanism (MCM v3.3.1), including furan chemistry (Coggon et al., 2019), and constrained to airborne measurements collected from Segment B (in-plume only) from the Williams Flats Fire. Also shown on this plot is the dashed line representing the impact of dilution - numerical or otherwise. The dilution always leads to a reduction in the maximum O_3 formation potential, but the magnitude of such reduction depends on the chemical regime. As shown, the dilution line for the Williams Flats Fire is close to the "ridge" (transition between NO_x/VOC-sensitive regimes), and hence dilution would lead to a rapid decrease in O_3 formation potential, and perhaps a change in the chemical regime as well (from NO_x-saturated/VOC-sensitive regime to the VOC-saturate/NO_x-sensitive regime).

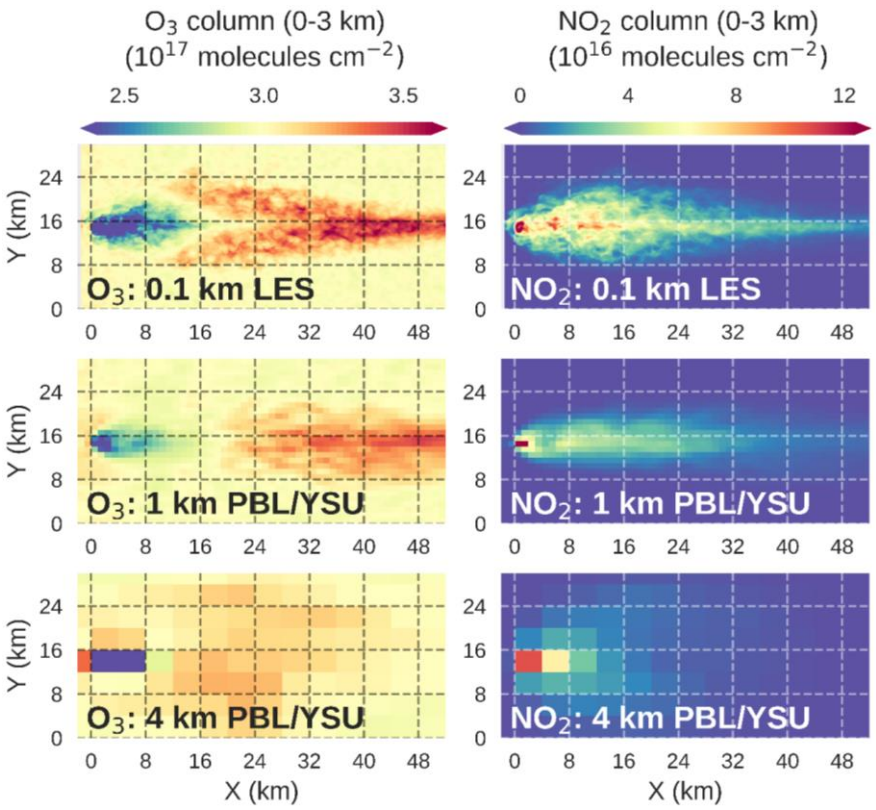

Figure 15. Modeled lower tropospheric column densities of O_3 and NO_2 with horizontal resolution of 0.1 km, 1km, and 4 km. All column densities are integrated from the surface to 3 km. The 0.1 km resolution model is the LES model that is discussed throughout this work, while the 1 km and the 4 km models are using YSU scheme and are driven by the same fire emissions but regridded accordingly. Other configurations in the 1km and 4 km models are identical to the 0.1 km model. See main text for more details.

Figure 15 illustrates the impact of model grid resolution on fire-induced column O_3 and NO_2, by comparing the results from the 0.1-km LES model to that from two model configurations with coarser horizontal resolutions: 1 km and 4 km. The 1-km and 4-km models shown in Figure 15 are configured in the same way as the 0.1-km LES model, except the fire emissions are re-gridded to 1 km and 4 km grids accordingly (mass conserved), and the Yonsei University (YSU) planetary boundary layer (PBL) scheme (Hong et al., 2006) are used in the 1 km and 4 km models.

As discussed before, the underlying principle of LES sets the upper limit to the grid spacing to about 0.1 km, therefore a grid spacing of 1 km or 4 km is inappropriate for LES.

As shown, the 0.1 km model reveals O_3 suppression in the first ~14 km or so, and O_3 enhancement is visible starting from ~14 km. At X = 40-50 km, the predicted O_3 column reaches ~3.71×10^{17} molecule cm^{-2} in the 0.1 km model, or ~0.70×10^{17} molecule cm^{-2} higher than the background O_3 column (~3.01×10^{17} molecule cm^{-2}). Both the 1 km and 4 km models capture the O_3 suppression in the first ~10 km or so. However, the maximum O_3 enhancement in the 4 km model appears at X = 16-28 km at ~3.27×10^{17} molecule cm^{-2}, or 0.27×10^{17} molecule cm^{-2} higher than the background, and the O_3 enhancement quickly diminished beyond X = ~32 km. That is, the 4 km model does not efficiently transport the fire-emitted O_3 precursors, and the column O_3 enhancement is underestimated by 61%. The 1 km model better captures the maximum O_3 enhancement (~3.47×10^{17} molecule cm^{-2}, or ~0.46×10^{17} molecule cm^{-2} above the background level, 34% lower than the 0.1 km LES model). NO_2 column shows similar trends as well: the 4 km model shows a fire-induced NO_2 column enhancement only in the first ~20 km or so, while the 0.1 km model efficiently transports the fire-induced NO_2 column to > 40 km. The 1 km model also better captures the spatial variation of the NO_2 column in the downwind direction. Interestingly, all three models are driven by the same external forcing, yet the plume in the 4 km model is much wider than that in the 0.1 km LES model, possibly due to numerical diffusion (a known issue in finite volume Eulerian grids). The 1 km model appears to predict a narrower plume width than the 0.1 km LES model. This is mainly because of the alignment of the fire source. In the 0.1 km LES model, in order to match the observed plume width (Figure 6 and Figure S4-S8), the fire source is tuned into a rectangular shape of 0.3 km (X) × 2.2 km (Y), while in the 1 km model the

fire source is just one 1 km × 1 km grid. The high horizontal resolution of the 0.1 km LES model allows a better representation of the shape and the orientation of the fire source as well. Overall, this exercise shows results that are consistent with those in Figure 14, that the numerical dilution leads to a decrease in O_3 formation potential, with a reduced efficiency of transporting smoke to the downwind direction. The 1 km model performs better than the 4 km model in terms of efficiently transporting the smoke and predicting the O_3 formation.

8. WHAT HORIZONTAL RESOLUTION SHOULD AIR QUALITY MODELS TARGET?

The effects of spatial resolution on the chemical evolution in biomass burning plumes or similar point-/area-sources have been discussed (Alvarado et al., 2009; Valin et al., 2011; van Wees & van der Werf, 2019). In particular, Valin et al. (2011) pointed out that in order to capture the NO_2 removal in the urban plumes, the model resolution has to be in the range of 4-12 km. Most active wildland fires areas are smaller than the urban scale. According to the Fire INventory from NCAR (FINN) version 2 (Wiedinmyer et al., 2011), a widely used biomass burning inventory, 90% of wildfires in 2019 were smaller than 1 km^2 (fire size). Therefore, the impacts of small fires on O_3 formation may be largely reduced (possibly entirely missing) in models with coarser spatial resolutions, which is caused by numerical dilution, a bias purely caused by grid resolution.

To what degree small fires affect air quality on the regional scale remains unclear. Yu et al. (2016) examined the model grid resolution effect on NO_x and O_3 in the Southeast U.S., with horizontal resolution varying from 0.25° × 0.3125° to 4° × 5°, and concluded that *"the good agreement of simulated and observed concentration variances implies that smaller-scale non-linearities (urban and power plant plumes) are not important on the regional scale"* (Yu et al.,

694 2016). Although Yu et al. (2016) did not specifically target wildfire influence, from the modeling
695 point-of-view, wildland fire sources are conceptually similar to urban and power plant sources.
696 Based on the sensitivity test in Figure 15, we argue that impacts of small wildfires on the regional
697 scale may not be captured in their $0.25^o \times 0.3125^o$ model (horizontal resolution: ~20 km).

698 To represent the smoke transport and O_3 formation associated with wildland fires, in
699 principle, the model grid resolution should be comparable to the active fire source. Although
700 plausible, it remains computationally challenging to perform simulations with LES schemes at
701 regional scale. Considering the computational cost associated with model resolution, we propose
702 that air quality forecast models should target ~1 km horizontal resolution in the near future. We
703 show in this work that a 1 km model can reasonably well capture the transport of NO_x and O_3
704 formation associated with a fire area that is ~60% of the grid size. Based again on FINN version 2,
705 in 2019, approximately 17% of wildfires in the U.S. are larger than 0.6 km^2, and these top 17%
706 wildfires contribute 62% total fire-NO_x emission, 60% total fire-CO emission, and 61% total non-
707 methane VOC emissions from fires nationwide. Therefore, an air quality forecast model with ~1
708 km horizontal resolution can greatly improve our ability to predict wildfire impacts on air quality,
709 which could potentially affect nearly half of the U.S. population (Figure S11). Additional benefit
710 of 1 km horizontal resolution is that the impacts of urban emissions will also be better resolved
711 (Valin et al., 2011).

712

713 **9. CONCLUSIONS AND REMARKS**

714 In this work, a high-resolution turbulence-resolving model, WRF-LES, is coupled to
715 chemistry to study the chemical evolution in a wildland fire plume. The results are evaluated

using airborne measurements collected from the Williams Flats Fire during the FIREX-AQ field campaign. The model reveals remarkable chemical heterogeneity that is supported by observations. Major findings are summarized as follows:

1. The strong heat released from the fire source drives rapid plume rise in the very early stage, which also leads to rapid dilution with background air. Dilution and physical mixing greatly affects chemistry inside the plume.

2. O_3 shows considerable heterogeneity inside the plume: suppressed at the center (due to NO reaction) but may be enhanced at the edges. To our knowledge, our model is the first to capture the observed cross-transect O_3 variations in optically thick biomass burning plumes.

3. PAN and maleic anhydride (from the oxidation of furan, a distinct class of compounds emitted from fires) are also enhanced at the edges of the plume in the early stage, implying faster OH oxidation at the edges. The OH enhancement at the plume edges is largely diminished in the later stage, mainly because the suppression of photochemistry inside the plume becomes weaker due to dilution.

4. Primary OH production is dominated by HONO photolysis, and HO_x cycling extends OH radicals deeper into the plume. Although OH oxidation is the major sink of VOCs in daytime plumes, we show that dark chemistry driven by O_3 and NO_3 oxidation may proceed at the same time but mostly in the lower part of (or below) thick plumes.

5. Although this modeling work cannot provide direct evidence of secondary HONO production in the studied plume, we find that observed HONO variability can be best explained by including a secondary HONO production from NO_2 heterogeneous reaction on aerosols.

737 We acknowledge that the model configuration is highly idealized, and much of the
738 observations remain unexplained by the model. Nevertheless, there are several key take-away
739 messages worth mentioning. Firstly, Lagrangian-type models that explore the chemical evolution
740 in dense fire plumes must specify the plume region being modeled, since it is the edges that
741 largely drive the photochemistry in thick fire plumes. Secondly, dilution and mixing within the
742 plume are important, which are not constant and may greatly affect how fast chemistry proceeds
743 inside the plume. Thirdly, we found that HONO and the photons that can trigger HONO photolysis
744 (represented by j_{HONO}) are always segregated in the modeled plume, i.e., HONO is always
745 depleted in the edges and the upper part, while j_{HONO} is exclusively elevated in the edges and
746 upper most part of the optically dense smoke (Figure 5). This has implications for satellite HONO
747 retrievals. Recently Theys et al. (2020) reported the detection of HONO in biomass burning
748 plumes from TROPOspheric Monitoring Instrument (TROPOMI), showcasing the remarkable
749 capability of retrieving reactive trace gases such as HONO from this space-borne instrument. High
750 resolution models with chemistry such as the LES-chemistry model used in this work can better
751 resolve the plume structure and the distributions of trace gases and aerosols, therefore may be
752 used to test remote sensing retrievals for optically dense plumes.

753 Lastly, we showed that model spatial resolution may shift the chemical regime and lead
754 to reduced O_3 formation potential. For the Williams Flats Fire studied in this work, a model with
755 ~1 km horizontal resolution may decently capture the fire-induced O_3 and NO_2 enhancement in
756 the downwind direction, but a model with ~4 km horizontal resolution may be insufficient to
757 capture the impacts on these short-lived pollutants. We thus propose that regional or national
758 air quality models in the U.S. should target ~1 km horizontal resolution in the near future, which

759 may greatly improve our capability to predict the wildfire impacts on air quality for nearly half of
760 the U.S. population.
761

762 **ACKNOWLEDGEMENTS AND DATA AVAILABILITY**

763 S.-Y. W. is partially supported by the FIREX-AQ project (80NSSC18K0681). S.R.H. and K.U.
764 and partially supported by the NASA FIREX-AQ project (80NSSC18K0638). The computing and
765 data storage resources, including the Cheyenne supercomputer (doi:10.5065/D6RX99HX), were
766 provided by the Computational and Information Systems Laboratory (CISL) at NCAR. NCAR is a
767 major facility sponsored by the NSF under Cooperative Agreement No. 1852977. We thank the
768 FIREX-AQ Science Team for their exceptional professionalism in support of this mission. We thank
769 Glenn Wolfe, Thomas Hanisco (NASA Goddard), Joshua P. Schwarz, Joseph M. Katich (NOAA/CSL),
770 Jose-Luis Jimenez, Pedro Campuzano-Jost, Douglas Day, Hongyu Guo, Demetrios Pagonis, Mindy
771 Schueneman (CU Boulder), and Alan Fried (CU Boulder) for their efforts in collecting the
772 measurements. Stuart McKeen, Rebecca Schwantes (CIRES/NOAA CSL), Brian McDonald, and
773 Gregory Frost (NOAA CSL) are acknowledged for helpful discussion. We thank Jimy Dudhia and
774 Mary Barth (NCAR) for the support regarding the LES modeling. The FIREX-AQ campaign data is
775 archived and available from NASA Langley Research Center (https://www-
776 air.larc.nasa.gov/missions/firex-aq/). The WRF model is available from github
777 (https://github.com/wrf-model/WRF).
778

779 **REFERENCES**

780 Abatzoglou, J. T., & Williams, A. P. (2016). Impact of anthropogenic climate change on wildfire
781 across western US forests. *Proceedings of the National Academy of Sciences*, *113*(42),
782 11770–11775. https://doi.org/10.1073/pnas.1607171113
783 Agee, E., & Gluhovsky, A. (1999). LES Model Sensitivities to Domains, Grids, and Large-Eddy
784 Timescales. *Journal of Atmospheric Sciences*, *56*(4), 599–604.
785 https://doi.org/10.1175/1520-0469(1999)056<0599:LMSTDG>2.0.CO;2
786 Alvarado, M. J., Logan, J. A., Mao, J., Apel, E., Riemer, D., Blake, D., et al. (2010). Nitrogen oxides
787 and PAN in plumes from boreal fires during ARCTAS-B and their impact on ozone: an
788 integrated analysis of aircraft and satellite observations. *Atmospheric Chemistry and*
789 *Physics*, *10*(20), 9739–9760. https://doi.org/10.5194/acp-10-9739-2010
790 Alvarado, M. J., Lonsdale, C. R., Yokelson, R. J., Akagi, S. K., Coe, H., Craven, J. S., et al. (2015).
791 Investigating the links between ozone and organic aerosol chemistry in a biomass
792 burning plume from a prescribed fire in California chaparral. *Atmospheric Chemistry and*
793 *Physics*, *15*(12), 6667–6688. https://doi.org/10.5194/acp-15-6667-2015
794 Alvarado, Matthew James, & Prinn, R. G. (2009). Formation of ozone and growth of aerosols in
795 young smoke plumes from biomass burning: 1. Lagrangian parcel studies. *Journal of*
796 *Geophysical Research: Atmospheres*, *114*(D9). https://doi.org/10.1029/2008JD011144

797 Alvarado, Matthew James, Wang, C., & Prinn, R. G. (2009). Formation of ozone and growth of
798 aerosols in young smoke plumes from biomass burning: 2. Three-dimensional Eulerian
799 studies. *Journal of Geophysical Research: Atmospheres*, *114*(D9).
800 https://doi.org/10.1029/2008JD011186
801 Ammann, M., Cox, R. A., Crowley, J. N., Jenkin, M. E., Mellouki, A., Rossi, M. J., et al. (2013).
802 Evaluated kinetic and photochemical data for atmospheric chemistry: Volume VI –
803 heterogeneous reactions with liquid substrates. *Atmospheric Chemistry and Physics*,
804 *13*(16), 8045–8228. https://doi.org/10.5194/acp-13-8045-2013
805 Andreae, M. O. (2019). Emission of trace gases and aerosols from biomass burning – an
806 updated assessment. *Atmospheric Chemistry and Physics*, *19*(13), 8523–8546.
807 https://doi.org/10.5194/acp-19-8523-2019
808 Brock, C. A., Washenfelder, R. A., Trainer, M., Ryerson, T. B., Wilson, J. C., Reeves, J. M., et al.
809 (2002). Particle growth in the plumes of coal-fired power plants. *Journal of Geophysical*
810 *Research: Atmospheres*, *107*(D12), AAC 9-1-AAC 9-14.
811 https://doi.org/10.1029/2001JD001062
812 Coen, J. (2013). Modeling wildland fires : A description of the Coupled Atmosphere-Wildland
813 Fire Environment model (CAWFE). https://doi.org/10.5065/D6K64G2G
814 Coggon, M. M., Lim, C. Y., Koss, A. R., Sekimoto, K., Yuan, B., Gilman, J. B., et al. (2019). OH
815 chemistry of non-methane organic gases (NMOGs) emitted from laboratory and
816 ambient biomass burning smoke: evaluating the influence of furans and oxygenated
817 aromatics on ozone and secondary NMOG formation. *Atmospheric Chemistry and*
818 *Physics*, *19*(23), 14875–14899. https://doi.org/10.5194/acp-19-14875-2019
819 Doerr, S. H., & Santín, C. (2016). Global trends in wildfire and its impacts: perceptions versus
820 realities in a changing world. *Philosophical Transactions of the Royal Society B: Biological*
821 *Sciences*, *371*(1696), 20150345. https://doi.org/10.1098/rstb.2015.0345
822 Fischer, E V, Jacob, D. J., Yantosca, R. M., Sulprizio, M. P., Millet, D. B., Mao, J., et al. (2014).
823 Atmospheric peroxyacetyl nitrate (PAN): a global budget and source attribution. *Atmos.*
824 *Chem. Phys.*, *14*(5), 2679–2698. https://doi.org/10.5194/acp-14-2679-2014
825 Fischer, Emily V., Zhu, L., Payne, V. H., Worden, J. R., Jiang, Z., Kulawik, S. S., et al. (2018). Using
826 TES retrievals to investigate PAN in North American biomass burning plumes.
827 *Atmospheric Chemistry and Physics*, *18*(8), 5639–5653. https://doi.org/10.5194/acp-18-
828 5639-2018
829 Flannigan, M., Cantin, A. S., de Groot, W. J., Wotton, M., Newbery, A., & Gowman, L. M. (2013).
830 Global wildland fire season severity in the 21st century. *Forest Ecology and*
831 *Management*, *294*, 54–61. https://doi.org/10.1016/j.foreco.2012.10.022
832 Hodshire, A. L., Bian, Q., Ramnarine, E., Lonsdale, C. R., Alvarado, M. J., Kreidenweis, S. M., et al.
833 (2019). More Than Emissions and Chemistry: Fire Size, Dilution, and Background Aerosol
834 Also Greatly Influence Near-Field Biomass Burning Aerosol Aging. *Journal of Geophysical*
835 *Research: Atmospheres*, *124*(10), 5589–5611. https://doi.org/10.1029/2018JD029674
836 Hodshire, Anna L., Akherati, A., Alvarado, M. J., Brown-Steiner, B., Jathar, S. H., Jimenez, J. L., et
837 al. (2019). Aging Effects on Biomass Burning Aerosol Mass and Composition: A Critical
838 Review of Field and Laboratory Studies. *Environmental Science & Technology*, *53*(17),
839 10007–10022. https://doi.org/10.1021/acs.est.9b02588

Hong, S.-Y., Noh, Y., & Dudhia, J. (2006). A New Vertical Diffusion Package with an Explicit Treatment of Entrainment Processes. *Monthly Weather Review*, *134*(9), 2318–2341. https://doi.org/10.1175/MWR3199.1

Jaffe, D. A., Wigder, N., Downey, N., Pfister, G., Boynard, A., & Reid, S. B. (2013). Impact of Wildfires on Ozone Exceptional Events in the Western U.S. *Environmental Science & Technology*, *47*(19), 11065–11072. https://doi.org/10.1021/es402164f

Jaffe, D. A., O'Neill, S. M., Larkin, N. K., Holder, A. L., Peterson, D. L., Halofsky, J. E., & Rappold, A. G. (2020). Wildfire and prescribed burning impacts on air quality in the United States. *Journal of the Air & Waste Management Association*, *70*(6), 583–615. https://doi.org/10.1080/10962247.2020.1749731

Knote, C., Hodzic, A., Jimenez, J. L., Volkamer, R., Orlando, J. J., Baidar, S., et al. (2014). Simulation of semi-explicit mechanisms of SOA formation from glyoxal in aerosol in a 3-D model. *Atmospheric Chemistry and Physics*, *14*(12), 6213–6239.

Kodros, J. K., Papanastasiou, D. K., Paglione, M., Masiol, M., Squizzato, S., Florou, K., et al. (2020). Rapid dark aging of biomass burning as an overlooked source of oxidized organic aerosol. *Proceedings of the National Academy of Sciences*. https://doi.org/10.1073/pnas.2010365117

Konovalov, I. B., Beekmann, M., Golovushkin, N. A., & Andreae, M. O. (2019). Nonlinear behavior of organic aerosol in biomass burning plumes: a microphysical model analysis. *Atmospheric Chemistry and Physics*, *19*(19), 12091–12119. https://doi.org/10.5194/acp-19-12091-2019

Koss, A. R., Sekimoto, K., Gilman, J. B., Selimovic, V., Coggon, M. M., Zarzana, K. J., et al. (2018). Non-methane organic gas emissions from biomass burning: identification, quantification, and emission factors from PTR-ToF during the FIREX 2016 laboratory experiment. *Atmospheric Chemistry and Physics*, *18*(5), 3299–3319. https://doi.org/10.5194/acp-18-3299-2018

Li, F., Zhang, X., Kondragunta, S., Schmidt, C. C., & Holmes, C. D. (2020). A preliminary evaluation of GOES-16 active fire product using Landsat-8 and VIIRS active fire data, and ground-based prescribed fire records. *Remote Sensing of Environment*, *237*, 111600. https://doi.org/10.1016/j.rse.2019.111600

Liu, X., Huey, L. G., Yokelson, R. J., Selimovic, V., Simpson, I. J., Müller, M., et al. (2017). Airborne measurements of western U.S. wildfire emissions: Comparison with prescribed burning and air quality implications. *Journal of Geophysical Research: Atmospheres*, *122*(11), 6108–6129. https://doi.org/10.1002/2016JD026315

Lu, X., Zhang, L., Yue, X., Zhang, J., Jaffe, D. A., Stohl, A., et al. (2016). Wildfire influences on the variability and trend of summer surface ozone in the mountainous western United States. *Atmospheric Chemistry and Physics*, *16*(22), 14687–14702. https://doi.org/10.5194/acp-16-14687-2016

Mandel, J., Beezley, J. D., & Kochanski, A. K. (2011). Coupled atmosphere-wildland fire modeling with WRF 3.3 and SFIRE 2011. *Geoscientific Model Development*, *4*(3), 591–610. https://doi.org/10.5194/gmd-4-591-2011

Martinuzzi, S., Stewart, S. I., Helmers, D. P., Mockrin, M. H., Hammer, R. B., & Radeloff, V. C. (2015). The 2010 wildland-urban interface of the conterminous United States. *Research Map NRS-8. Newtown Square, PA: U.S. Department of Agriculture, Forest Service,*

884 *Northern Research Station. 124 p. [Includes Pull-out Map].*, *8*, 1–124.
885 https://doi.org/10.2737/NRS-RMAP-8
886 Mason, S. A., Trentmann, J., Winterrath, T., Yokelson, R. J., Christian, T. J., Carlson, L. J., et al.
887 (2006). Intercomparison of Two Box Models of the Chemical Evolution in Biomass-
888 Burning Smoke Plumes. *Journal of Atmospheric Chemistry*, *55*(3), 273–297.
889 https://doi.org/10.1007/s10874-006-9039-5
890 McClure, C. D., & Jaffe, D. A. (2018). US particulate matter air quality improves except in
891 wildfire-prone areas. *Proceedings of the National Academy of Sciences*, *115*(31), 7901–
892 7906. https://doi.org/10.1073/pnas.1804353115
893 Moeng, C.-H., Dudhia, J., Klemp, J., & Sullivan, P. (2007). Examining Two-Way Grid Nesting for
894 Large Eddy Simulation of the PBL Using the WRF Model. *Monthly Weather Review*,
895 *135*(6), 2295–2311. https://doi.org/10.1175/MWR3406.1
896 Palm, B. B., Peng, Q., Fredrickson, C. D., Lee, B. H., Garofalo, L. A., Pothier, M. A., et al. (2020).
897 Quantification of organic aerosol and brown carbon evolution in fresh wildfire plumes.
898 *Proceedings of the National Academy of Sciences*, *117*(47), 29469–29477.
899 https://doi.org/10.1073/pnas.2012218117
900 Parrington, M., Palmer, P. I., Lewis, A. C., Lee, J. D., Rickard, A. R., Di Carlo, P., et al. (2013).
901 Ozone photochemistry in boreal biomass burning plumes. *Atmospheric Chemistry and*
902 *Physics*, *13*(15), 7321–7341. https://doi.org/10.5194/acp-13-7321-2013
903 Peng, Q., Palm, B. B., Melander, K. E., Lee, B. H., Hall, S. R., Ullmann, K., et al. (2020). HONO
904 Emissions from Western U.S. Wildfires Provide Dominant Radical Source in Fresh
905 Wildfire Smoke. *Environmental Science & Technology*, *54*(10), 5954–5963.
906 https://doi.org/10.1021/acs.est.0c00126
907 Reid Colleen E., Brauer Michael, Johnston Fay H., Jerrett Michael, Balmes John R., & Elliott
908 Catherine T. (2016). Critical Review of Health Impacts of Wildfire Smoke Exposure.
909 *Environmental Health Perspectives*, *124*(9), 1334–1343.
910 https://doi.org/10.1289/ehp.1409277
911 Roberts, J. M., Stockwell, C. E., Yokelson, R. J., de Gouw, J., Liu, Y., Selimovic, V., et al. (2020).
912 The nitrogen budget of laboratory-simulated western US wildfires during the FIREX 2016
913 Fire Lab study. *Atmospheric Chemistry and Physics*, *20*(14), 8807–8826.
914 https://doi.org/10.5194/acp-20-8807-2020
915 Roode, S. R. de, Duynkerke, P. G., & Jonker, H. J. J. (2004). Large-Eddy Simulation: How Large is
916 Large Enough? *Journal of Atmospheric Sciences*, *61*(4), 403–421.
917 https://doi.org/10.1175/1520-0469(2004)061<0403:LSHLIL>2.0.CO;2
918 Schwarz, J. P., Gao, R. S., Spackman, J. R., Watts, L. A., Thomson, D. S., Fahey, D. W., et al.
919 (2008). Measurement of the mixing state, mass, and optical size of individual black
920 carbon particles in urban and biomass burning emissions. *Geophysical Research Letters*,
921 *35*(13). https://doi.org/10.1029/2008GL033968
922 Singh, H. B., Cai, C., Kaduwela, A., Weinheimer, A., & Wisthaler, A. (2012). Interactions of fire
923 emissions and urban pollution over California: Ozone formation and air quality
924 simulations. *Atmospheric Environment*, *56*, 45–51.
925 https://doi.org/10.1016/j.atmosenv.2012.03.046

Theys, N., Volkamer, R., Müller, J.-F., Zarzana, K. J., Kille, N., Clarisse, L., et al. (2020). Global nitrous acid emissions and levels of regional oxidants enhanced by wildfires. *Nature Geoscience*, *13*(10), 681–686. https://doi.org/10.1038/s41561-020-0637-7

Tie, X., Madronich, S., Walters, S., Zhang, R., Rasch, P., & Collins, W. (2003). Effect of clouds on photolysis and oxidants in the troposphere. *Journal of Geophysical Research: Atmospheres*, *108*(D20). https://doi.org/10.1029/2003JD003659

Trentmann, J., Andreae, M. O., Graf, H.-F., Hobbs, P. V., Ottmar, R. D., & Trautmann, T. (2002). Simulation of a biomass-burning plume: Comparison of model results with observations. *Journal of Geophysical Research: Atmospheres*, *107*(D2), AAC 5-1-AAC 5-15. https://doi.org/10.1029/2001JD000410

Trentmann, Jörg, Andreae, M. O., & Graf, H.-F. (2003). Chemical processes in a young biomass-burning plume. *Journal of Geophysical Research: Atmospheres*, *108*(D22). https://doi.org/10.1029/2003JD003732

Trentmann, Jörg, Früh, B., Boucher, O., Trautmann, T., & Andreae, M. O. (2003). Three-dimensional solar radiation effects on the actinic flux field in a biomass-burning plume. *Journal of Geophysical Research: Atmospheres*, *108*(D17). https://doi.org/10.1029/2003JD003422

Trentmann, Jörg, Yokelson, R. J., Hobbs, P. V., Winterrath, T., Christian, T. J., Andreae, M. O., & Mason, S. A. (2005). An analysis of the chemical processes in the smoke plume from a savanna fire. *Journal of Geophysical Research: Atmospheres*, *110*(D12). https://doi.org/10.1029/2004JD005628

Valin, L. C., Russell, A. R., Hudman, R. C., & Cohen, R. C. (2011). Effects of model resolution on the interpretation of satellite NO_2 observations. *Atmospheric Chemistry and Physics*, *11*(22), 11647–11655. https://doi.org/10.5194/acp-11-11647-2011

van Wees, D., & van der Werf, G. R. (2019). Modelling biomass burning emissions and the effect of spatial resolution: a case study for Africa based on the Global Fire Emissions Database (GFED). *Geoscientific Model Development*, *12*(11), 4681–4703. https://doi.org/10.5194/gmd-12-4681-2019

Westerling, A. L., Hidalgo, H. G., Cayan, D. R., & Swetnam, T. W. (2006). Warming and Earlier Spring Increase Western U.S. Forest Wildfire Activity. *Science*, *313*(5789), 940–943. https://doi.org/10.1126/science.1128834

Wiedinmyer, C., Akagi, S. K., Yokelson, R. J., Emmons, L. K., Al-Saadi, J. A., Orlando, J. J., & Soja, A. J. (2011). The Fire INventory from NCAR (FINN): a high resolution global model to estimate the emissions from open burning. *Geosci. Model Dev.*, *4*(3), 625–641. https://doi.org/10.5194/gmd-4-625-2011

Yokelson, R. J., Christian, T. J., Karl, T. G., & Guenther, A. (2008). The tropical forest and fire emissions experiment: laboratory fire measurements and synthesis of campaign data. *Atmospheric Chemistry and Physics*, *8*(13), 3509–3527. https://doi.org/10.5194/acp-8-3509-2008

Yu, K., Jacob, D. J., Fisher, J. A., Kim, P. S., Marais, E. A., Miller, C. C., et al. (2016). Sensitivity to grid resolution in the ability of a chemical transport model to simulate observed oxidant chemistry under high-isoprene conditions. *Atmospheric Chemistry and Physics*, *16*(7), 4369–4378. https://doi.org/10.5194/acp-16-4369-2016